LAWRENCE
LIVERMORE
NATIONAL
LABORATORY

LLNL-JRNL-864669

Statistical data analysis of x-ray spectroscopy data enabled by neural network accelerated Bayesian inference

M. J. MacDonald, B. A. Hammel, B. Bachmann, M. Bitter, P. Efthimion, J. A. Gaffney, L. Gao, B. D. Hammel, K. W. Hill, B. F. Kraus, A. G. MacPhee, L. Peterson, M. B. Schneider, H. A. Scott, D. B. Thorn, C. B. Yeamans

May 21, 2024

Review of Scientific Instruments

Disclaimer

Statistical data analysis of x-ray spectroscopy data enabled by neural network accelerated Bayesian inference

M. J. MacDonald,[1, a)] B. A. Hammel,[1] B. Bachmann,[1] M. Bitter,[2] P. Efthimion,[2] J. A. Gaffney,[1] L. Gao,[2] B. D. Hammel,[3] K. W. Hill,[2] B. F. Kraus,[2] A. G. MacPhee,[1] L. Peterson,[1] M. B. Schneider,[1] H. A. Scott,[1] D. B. Thorn,[1] and C. B. Yeamans[1]

[1)] *Lawrence Livermore National Laboratory, Livermore, California 94550*

[2)] *Princeton Plasma Physics Laboratory, Princeton University, Princeton, NJ 08543*

[3)] *SambaNova Systems, Palo Alto, CA 94303, USA*

(Dated: 31 July 2024)

Bayesian inference applied to x-ray spectroscopy data analysis enables uncertainty quantification necessary to rigorously test theoretical models. However, when comparing to data, detailed atomic physics and radiation transfer calculations of x-ray emission from non-uniform plasma conditions are typically too slow to be performed inline with statistical sampling methods, such as Markov Chain Monte Carlo sampling. Furthermore, differences in transition energies and x-ray opacities often make direct comparisons between simulated and measured spectra unreliable. We present a spectral decomposition method that allows for corrections to line positions and bound-bound opacities to best fit experimental data, with the goal of providing quantitative feedback to improve the underlying theoretical models and guide future experiments. In this work, we use a neural network (NN) surrogate model to replace spectral calculations of isobaric hot-spots created in Kr-doped implosions at the National Ignition Facility. The NN was trained on calculations of x-ray spectra using an isobaric hot-spot model post-processed with Cretin, a multi-species atomic kinetics and radiation code. The speed up provided by the NN model to generate x-ray emission spectra enables statistical analysis of parametrized models with sufficient detail to accurately represent the physical system and extract the plasma parameters of interest.

I. INTRODUCTION

Uncertainty quantification is a critical aspect in the analysis of experimental data and is required to make meaningful comparisons between measurements and theoretical models. Given a set of experimental measurements and a theoretical model, Bayesian inference can provide rigorous statistical uncertainties in the model parameters, including correlations between parameters. Bayesian inference has been shown to be a powerful tool to analyze magnetic confinement fusion experiments[1–5] and has been more recently applied to HED and inertial confinement fusion experiments.[6–11] Careful consideration of these sensitivities and correlations is critical to correctly estimate errors when fitting experimental data.[12] Correlations can be particularly useful to analyze, as they can identify improvements to experimental designs by identifying how the uncertainties in key parameters are affected by other model parameters that may be under constrained.

Applying Bayesian inference to experimental data requires a sufficiently accurate model to describe the system that can be varied and sampled a large number of times to obtain adequate sampling statistics. These requirements often conflict, as model complexity and computational cost are directly related, necessitating methods to speed up model calculations whenever possible. Furthermore, fitting measured x-ray spectra using simulated spectra is often complicated by differences in line positions, which can be caused by errors in simulated spectra or the dispersion applied to experimental data and can dominate the fit metric if ignored. In such a case, the fitting routine will optimize the fit metric it has been given and return a solution that poorly fits the features of interest, such as line ratios or widths. A common approach to solve this problem is to compare integrated intensities within specific bands (e.g. line ratios), circumventing the issue by only comparing line intensities, however this method ignores potentially useful information such as line widths and becomes unreliable when spectral regions overlap.

In this paper, we present a method to perform Bayesian inference on experimental data using a neural network (NN) surrogate model to dramatically reduce the computational time to generate model predictions and define the NN to easily allow for adjustments to the model spectra necessary to fit the experimental data. This method is applied to time-integrated x-ray spectra from Kr-doped implosions at NIF to demonstrate the technique.

II. KR-DOPED IMPLOSIONS AT THE NIF

Here we consider time-integrated x-ray spectroscopy data from Kr-doped implosions at the NIF designed to provide detailed measurements of hot-spot conditions using Kr emission spectroscopy. The experiment (NIF shot N180423-002) used the pushered single shell (PSS) drive[13,14], an indirect-drive platform with relatively low ablation-front growth that has been re-

[a)] macdonald10@llnl.gov

LLNL-JRNL-864669

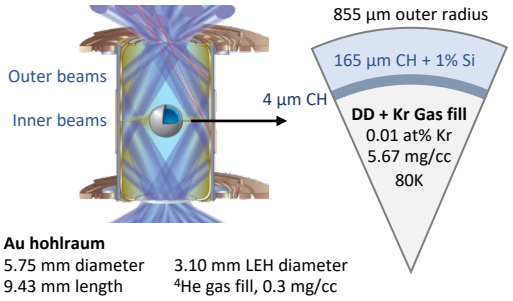

FIG. 1. Target design for the experimental platform showing the hohlraum dimensions and capsule specification.

fined through many tuning experiments to produce well-behaved, spherical implosions. The experiment used a gold hohlraum, 5.75 mm in diameter and 9.43 mm in length with 3.10 mm laser entrance holes (LEHs), as shown in Fig. 1. The capsule has an outer radius of 855 μm with a total ablator thickness of 169 μm, split into three layers. The outer layer consists of 165 μm of CH doped with 1% Si to prevent preheat from the hohlraum radiation and the inner 4 μm layer is undoped CH. The capsule gas fill is DD with 0.01 atomic % Kr at a density of 5.67 mg/cc (6975 torr) and the hohlraum is filled with ^{4}He at a density of 0.3 mg/cc (372 torr) fielded at a temperature of 80 K. For the purposes of line-emission spectroscopy, Kr dopant levels of 0.01–0.03 at. % are adequate to achieve sufficient signal levels and low enough to keep the Kr Heβ emission optically thin and not significantly impact implosion performance[15,16].

The time-integrated x-ray spectra were collected using two x-ray spectrometers fielded on the equatorial plane of the NIF target chamber, ConSpec[17,18] and dHIRES[19]. The NIF Continuum Spectrometer (ConSpec) is an absolutely calibrated Bragg crystal spectrometer with a conical highly annealed pyrolytic graphite crystal designed to measure the x-ray continuum in the energy range of 20 to 30 keV with 550 μm spatial resolution and spectral resolution of $E/\Delta E \sim 250$. The dHIRES diagnostic is a high-resolution x-ray spectrometer designed to measure both time-resolved and time-integrated Kr K-shell emission. dHIRES uses three crystals: two conical crystals to focus Heα and Heβ emission onto a single x-ray streak camera and a third crystal in the Von Hamos geometry with image plate for the detector to obtain an absolutely calibrated spectrum covering the full range of the time-resolved channels. The spectral resolution for the time-integrated channel is $E/\Delta E \sim 1170$.

III. HOTSPOT MODELING

Linking observations to physically meaningful quantities requires a model with input parameters that can be sampled to compare predictions to observables. To model the hot-spot emission in this analysis, we use a 1D isobaric hot-spot model derived by R. Betti *et al.*[20] The hot-spot model requires four parameters: the hot-spot radius (R), central temperature (T_0), density (ρ_0 or alternatively the electron density, n_{e0}), and a shell density (ρ_{sh}). The system of equations is given by

$$T(\hat{r}) = T_0 \frac{(1-\hat{r}^2)^{2/5}}{1-0.15\hat{r}^2}$$
$$\rho(\hat{r}) = \rho_0 \frac{1-0.15\hat{r}^2}{(1-\hat{r}^2)^{2/5}+\epsilon} \quad (1)$$

where $\hat{r} = r/R$ is the scaled radius and $\epsilon = 0.85\rho_0/\rho_{sh} \ll 1$ is an *ad hoc* term added to avoid a singularity at $\hat{r} = 1$ resulting from the assumption that T goes to zero at the hot-spot boundary used in the derivation of the model. Note that the temperature at $r = 0$ is T_0, however the electron density is not n_{e0} due to the parameter ϵ.

We model the x-ray emission for a given hot-spot profile using Cretin[21], a multi-species atomic kinetics and radiation transfer code. Cretin models the DD+Kr plasma self-consistently for a given plasma condition (n_e, T_e) with radiation transport to calculate emission from the 1D spherical hot-spot profiles. Modeling the system with 1D spherical profiles provides a significant improvement compared to fitting the "average" condition, which can be misleading if the sensitivities of each measurement are not carefully considered.[22] The multi-species Cretin calculations used a simple principal quantum number model for deuterium, while the Kr atomic model combined fine-structure data from the Flexible Atomic Code[23] for the H- through Be-like sequences with a screened-hydrogenic model[24] for other charge states.

IV. SPECTRAL DECOMPOSITION

A common challenge in fitting bound-bound x-ray spectra arises from differences in line energies between simulated spectra and measured results. These differences can be due to errors in the experimental data (e.g. spectral calibration), the simulated spectra (e.g. atomic data errors), or both. Regardless of the cause, small offsets between the data and the simulations can give rise to large fitting errors, especially when fitting narrow spectral features where small difference in line energies give rise to large contributions to the distance metric in the loss function (e.g. mean squared error).

To alleviate this issue, we decompose the simulated spectra into individual lines described by analytic functions, allowing corrections to be made to the line positions in the fitting process as described in a previous publication.[22] This process is similar to typical dimensional reduction methods used in many machine learning models, including similar methods to analyze x-ray spectra,[25] however this method allows for specific aspects of the spectra to be modified by well-defined parameters

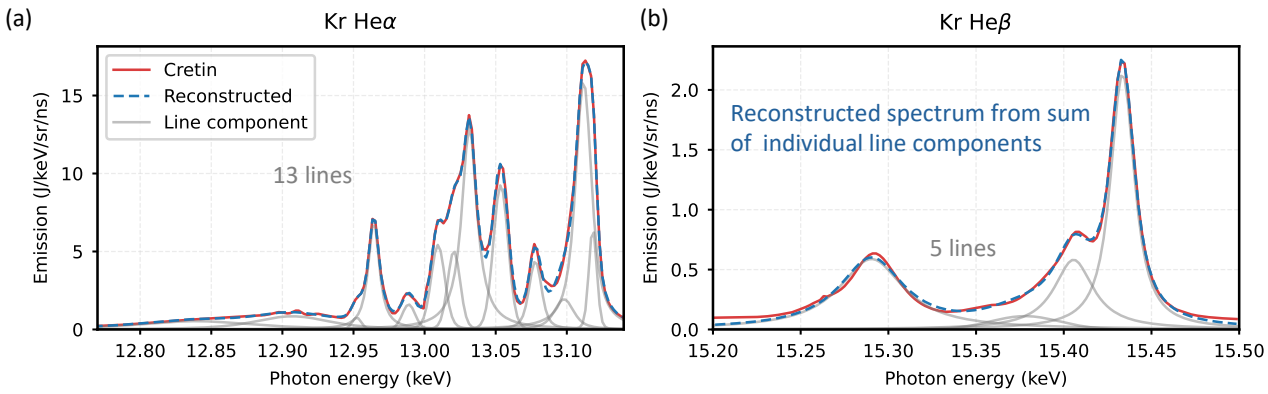

FIG. 2. Spectral decomposition of the (a) Kr Heα and (b) Heβ regions showing spectra calculated using Cretin in red, the reconstructed fit in dashed blue, and the individual Voigt line profiles in gray showing that the Cretin spectra can be accurately represented by a set of Voigt profiles.

such as line shifts, widths, and amplitudes. Importantly, when using this method to fit the data, the corrections required to match the experimental data can be extracted from the fit and used to improve the atomic modeling and spectral calibration with quantitative feedback to improve atomic data and opacity models. With the spectra decomposed into lines and other spectral features (e.g. backgrounds, edges) the simulated spectra can be defined by a set of input parameters, suitable for fitting using a Bayesian framework.

Here, we decompose the Kr Heα region into 13 lines and the Heβ region into 5 lines, all of which are assumed to be Voigt functions, each of which has 4 parameters. An example of the spectral decomposition results is shown in Fig. 2. This technique can be extended to use more sophisticated line profiles as long as they can be described using a defined set of parameters for decomposition and reconstruction. With the flexibility provided by this spectral decomposition method we can apply Bayesian inference to our data, allowing for adjustments necessary to describe the measured spectra to extract the hot-spot parameters of interest.

V. NEURAL NETWORK SURROGATE MODEL

For computationally expensive models, it can be prohibitively time consuming to perform statistical sampling to determine the uncertainties in the input parameters. Methods such as Markov Chain Monte Carlo (MCMC) sampling often take many thousands to millions of samples to converge, and the number of required samples typically increases exponentially with the number of input model parameters. Several previous studies have demonstrated the effectiveness of NN surrogate models to replace computationally expensive models for HED and fusion experiments.[7,26–29]

Producing spectra from a given hot-spot condition using Cretin and decomposing the data into the analytic features described above takes approximately 30 seconds using a 36-CPU high performance computer. If convergence for the MCMC sampling requires approximately one million samples run in series, convergence will take approximately one year of computational time (or weeks if using parallel MCMC chains with sufficient computing resources). By replacing the spectral generation code with a NN and designing the network to directly output the reconstruction parameters for each spectrum (e.g. Voigt line parameters), we can dramatically reduce the computational cost and time required to converge with MCMC sampling. A diagram showing how the NN replaces the spectral generation and line fitting is shown in Fig. 3.

To produce a set of training data for the NN surrogate model, 25,000 Cretin calculations were performed using 1D spherical hot-spot profiles. The training data were calculated by randomly sampling the hot-spot parameters over the ranges of R = 20–50 μm, T_0 = 3–6 keV, n_{e0} = (5-200)$\times 10^{23}$ cm^{-3}, and ρ_{sh} = 3–10 g/cm^3. The sampling for R, T_0, and ρ_{sh} were uniform in linear space while the sampling for n_{e0} was sampled uniformly in log space. These ranges are sufficient to span the probability distributions inferred in the final fitting of the data. In practice, if it is found that the probability distributions of any input parameters approach the limits of the training data, it is possible to add more training runs and repeat the process as necessary.

The NN was implemented using *pytorch*[30] using an architecture with 4 input nodes for the hot-spot parameters and 77 output nodes, corresponding to the reconstruction parameters required for the three spectral regions (53 for Kr Heα, 21 for Kr Heβ, and 3 for the continuum). The NN has 5 hidden layers with an increasing number of nodes (64, 128, 256, 512, and 1024) before reducing to the final output nodes. Each hidden layer includes a rectified linear unit activation unit and a dropout rate of 1% to reduce overfitting. This specific NN architecture was found to produce good results for our problem and

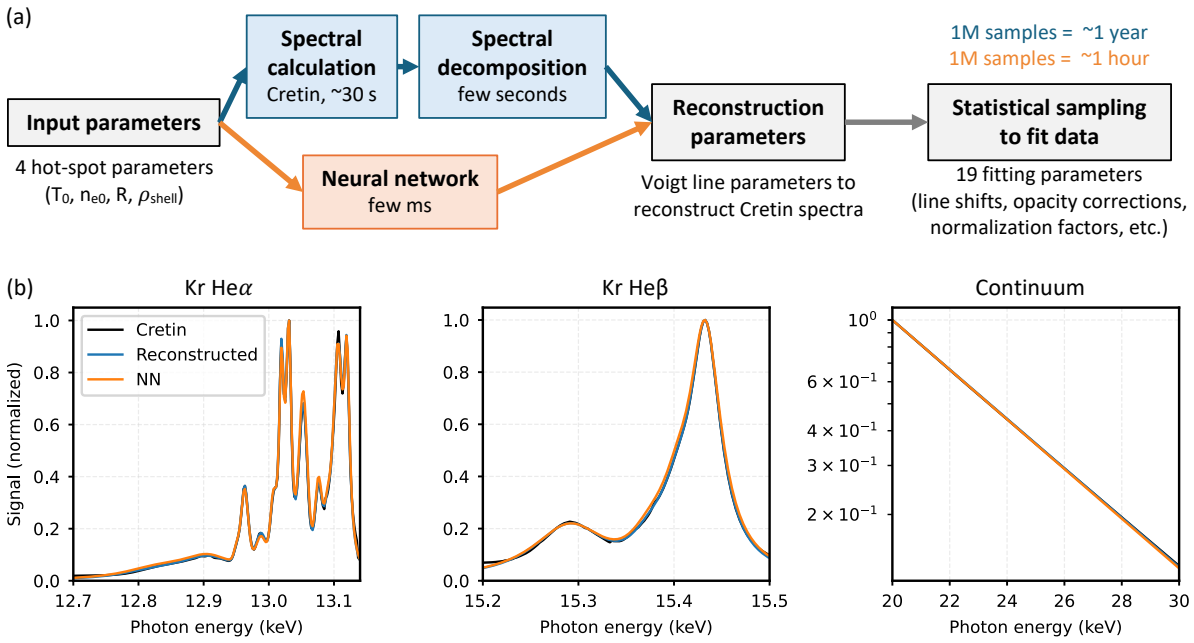

FIG. 3. (a) Fitting workflow showing where NN surrogate model replaces both the spectral calculations and spectral decomposition steps to reduce computational time. (b) Spectral reconstruction results compared to an example Cretin calculation (black) compared to reconstructed spectra directly from the spectral decomposition process (blue) and using the results of the NN surrogate model (orange).

other architectures with different numbers of hidden layers and layer widths were tested, although there is certainly room for optimization in this area. The NN was trained using the Adam optimization algorithm[31] with an adaptive learning rate using the mean absolute error (MAE) loss metric.

VI. FITTING EXPERIMENTAL DATA

Using the NN to produce simulated spectra for the four hot-spot profile parameters, we add additional parameters to compare the simulated spectra to the experimental data. These include corrections to the calculations such as line shifts to match spectral lines, amplitude multipliers to optically thick lines, and additional broadening of specific lines as well as typical corrections such as background levels and normalization factors. In total, this analysis uses 21 fitting adjustment parameters: 3 background level parameters, 3 normalization factors, 9 line shift parameters for the Kr Heα region, 2 line shifts for the Kr Heβ region, 2 opacity correction multipliers for lines in the Kr Heα region with significant optical depth leading to fitting issues (intercombination and resonance lines), and additional broadening for the emission line at 12.99 keV in the Heα spectrum.

It is important to note that the specific fitting parameters used in this analysis (e.g. which lines to allow to shift, which lines to include opacity multipliers) were determined to be sufficient to accurately fit the data, however other choices can be made with the trade-off of flexibility and computational cost by allowing for more free parameters. In practice, some amount of iteration is required to determine which parameters should be included in the fitting process and the prior for each parameter is set correctly. For example, if the line shift parameters are not properly bounded, it is possible for two lines to switch positions, leading to confusing results. Through this iteration, it is possible to identify which features in the data are not adequately represented by the model, and the additional parameters required are indicators of where the models may need to be improved.

We apply Bayesian inference to the data with MCMC sampling using the *emcee*[32] package implemented in Python. Samples were collected using 64 walkers and a normal likelihood with bounded uniform priors to restrict the input plasma parameters to the ranges used in the NN training data, to limit line energy shifts to prevent emission lines from swapping positions, and to enforce physical constraints (e.g. positive amplitude multipliers). To ensure convergence, 200,000 steps were run for each walker for a total of 12.8M samples (walkers $\times$ steps) and the first 150,000 steps were discarded as the burn-in phase of the MCMC sampling process.

Figure 4 shows the measured (a) Kr Heα, (b) Kr Heβ, and (c) continuum spectra in black with 20 samples from the inferred posterior distributions with (orange) and without (blue) fitting parameters included. For the Heα spectrum, the offset in the signal level in the photon energy range of 12.95–13.00 keV and the energy offset of

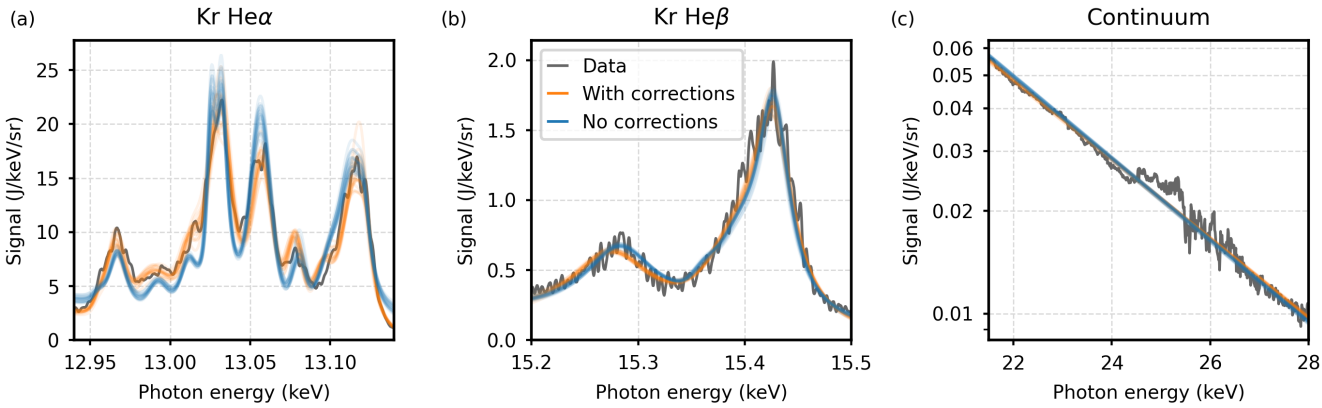

FIG. 4. 20 samples from the posterior distributions for the fitting results with (orange) and without (blue) fitting parameters compared to the experimental data from NIF shot N180423-002 (black) for the three spectral regions.

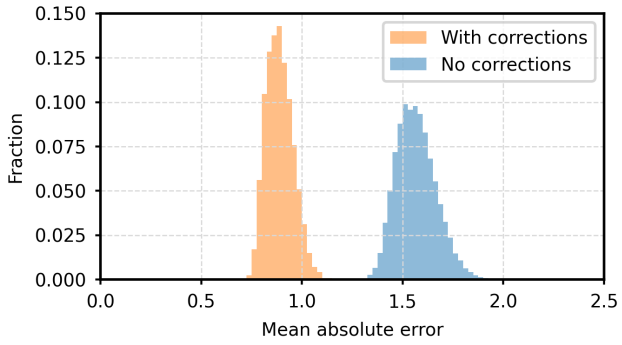

FIG. 5. Distribution of MAEs for the Kr Heα spectrum with (orange) and without (blue) the use of additional fitting adjustment parameters.

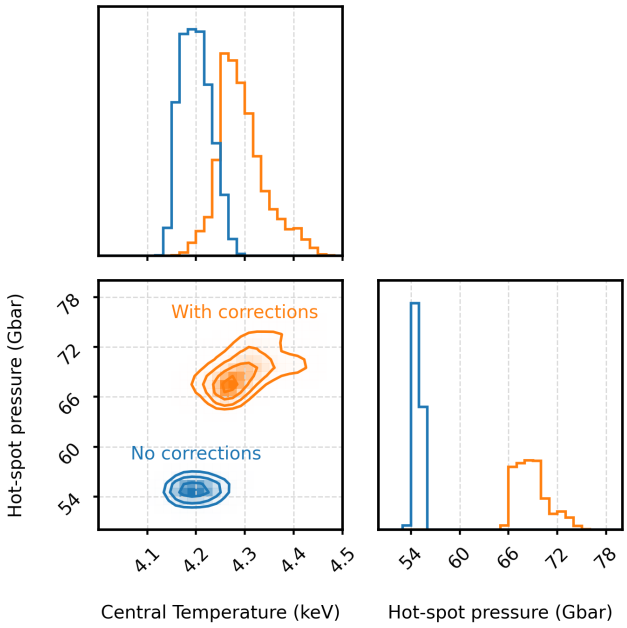

FIG. 6. Fitting results for the hot-spot central temperature and pressure, showing the probability distribution of each parameter along the top and the correlation of the two plasma parameters on the bottom left. The results with the additional fitting parameters are shown in orange and the results with no corrections are shown in blue.

the low energy side of the resonance line at 13.12 keV dominate the error calculated in the fitting procedure.

Quantifying the improvement using additional fitting parameters, the distributions for the MAEs of the fits for the Kr Heα spectrum are shown in Fig. 5, where the average value of the MAE is reduced from 1.57 to 0.89. More importantly, Fig. 6 shows the resulting change in inferred hot-spot temperature and pressure when the fitting parameters are included. While the improved analysis shows the central temperature of the hot-spot only changes by a few percent due to the strong constraint from the x-ray continuum, the inferred pressure of the hot-spot is nearly 25% higher when allowing for the fitting corrections. This example highlights the possible impact of the fitting adjustments, however more detailed analysis of the specific corrections applied to the calculated spectra will be required to verify that the corrections are appropriate. Ideally, these corrections can be used to improve the underlying models used in collisional radiative calculations.

VII. CONCLUSIONS

We presented a method to accurately fit x-ray spectra by decomposing simulations into individual lines and including energy shifts in the fitting process. This method naturally results in a large number of fitting parameters, necessitating the use of a NN surrogate model to increase the model sampling rate for statistical fitting. The method has been applied to time-integrated x-ray

spectra from a Kr-doped capsule implosion at the NIF, reducing the computational time required to fit the data from years to hours. Additional refinements to the model will improve the fitting results and the reduced computational cost of the NN surrogate model will enable statistical fitting of time-resolved hot-spot emission data. In this analysis we do not include error introduced by the NN surrogate model due to the fact that these errors are likely considerably smaller than other uncertainties in the spectral modeling process, however these errors can be included in the NN predictions.[27] Furthermore, this method can be extended to incorporate additional measurements (e.g. x-ray imaging, neutron diagnostics) and fit absolute emission values to x-ray spectra to better constrain theoretical models.

ACKNOWLEDGMENTS

This work was performed under the auspices of the U.S. Department of Energy by Lawrence Livermore National Laboratory under contract DE-AC52-07NA27344 and supported by Laboratory Directed Research and Development (LDRD) Grant Nos. 18-ERD-015, 22-ERD-005, and 22-FS-039.

VIII. DATA AVAILABILITY

The data that support the findings of this study are available from the corresponding author upon reasonable request.

[1] A. Pavone, A. Merlo, S. Kwak, and J. Svensson, Plasma Physics and Controlled Fusion **65**, 053001 (2023).
[2] J. Svensson, A. Werner, and J.-E. Contributors, Plasma Physics and Controlled Fusion **50**, 085002 (2008).
[3] D. Li, J. Svensson, H. Thomsen, F. Medina, A. Werner, and R. Wolf, Review of Scientific Instruments **84**, 083506 (2013).
[4] J. A. Romero, S. A. Dettrick, E. Granstedt, T. Roche, and Y. Mok, Nature Communications **9**, 691 (2018).
[5] S. Kwak, U. Hergenhahn, U. Höfel, M. Krychowiak, A. Pavone, J. Svensson, O. Ford, R. König, S. Bozhenkov, G. Fuchert, E. Pasch, K. J. Brunner, J. Knauer, P. Kornejew, H. Trimiño Mora, T. S. Pedersen, and W. .-X. Team, Review of Scientific Instruments **92**, 043505 (2021).
[6] P. F. Knapp and W. E. Lewis, Review of Scientific Instruments **94**, 061103 (2023).
[7] W. E. Lewis, P. F. Knapp, S. A. Slutz, P. F. Schmit, G. A. Chandler, M. R. Gomez, A. J. Harvey-Thompson, M. A. Mangan, D. J. Ampleford, and K. Beckwith, Physics of Plasmas **28**, 092701 (2021).
[8] J. Ruby, J. Gaffney, J. Rygg, Y. Ping, and G. Collins, Physics of Plasmas **28** (2021).
[9] P. F. Knapp, M. E. Glinsky, M. A. Schaeuble, C. A. Jennings, M. Evans, J. Gunning, T. J. Awe, G. A. Chandler, M. Geissel, M. R. Gomez, K. D. Hahn, S. B. Hansen, E. C. Harding, A. J. Harvey-Thompson, S. Humane, B. T. Klein, M. Mangan, T. Nagayama, A. J. Porwitzky, D. E. Ruiz, P. F. Schmit, S. A. Slutz, I. C. Smith, M. R. Weis, D. A. Yager-Elorriaga, D. J. Ampleford, K. Beckwith, T. R. Mattsson, K. J. Peterson, and D. B. Sinars, Physics of Plasmas **29**, 052711 (2022).
[10] W. E. Lewis, O. M. Mannion, D. E. Ruiz, C. A. Jennings, P. F. Knapp, M. R. Gomez, A. J. Harvey-Thompson, M. R. Weis, S. A. Slutz, D. J. Ampleford, and K. Beckwith, Physics of Plasmas **30**, 052701 (2023).
[11] B. A. Hammel, B. D. Hammel, H. A. Scott, and J. L. Peterson, High Energy Density Physics **50**, 101077 (2024).
[12] M. F. Kasim, T. P. Galligan, J. Topp-Mugglestone, G. Gregori, and S. M. Vinko, Phys. Plasmas **26**, 112706 (2019).
[13] R. Sacks, R. Tipton, and F. Graziani, J. Phys. Conf. Series **717**, 012076 (2016).
[14] E. L. Dewald, J. E. Pino, R. E. Tipton, J. D. Salmonson, J. Ralph, E. Hartouni, S. F. Khan, R. Hatarik, C. V. Young, D. Thorn, V. A. Smalyuk, R. Sacks, A. Nikroo, N. Rice, S. A. MacLaren, S. Prisbrey, B. A. Remington, and F. Graziani, Phys. Plasmas **26**, 072705 (2019).
[15] T. Ma, H. Chen, P. K. Patel, M. B. Schneider, M. A. Barrios, D. T. Casey, H. K. Chung, B. A. Hammel, L. F. Berzak Hopkins, L. C. Jarrott, S. F. Khan, B. Lahmann, R. Nora, M. J. Rosenberg, A. Pak, S. P. Regan, H. A. Scott, H. Sio, B. K. Spears, and C. R. Weber, Rev. Sci. Instrum. **87**, 1–5 (2016).
[16] H. Chen, T. Ma, R. Nora, M. A. Barrios, H. A. Scott, M. B. Schneider, L. Berzak Hopkins, D. T. Casey, B. A. Hammel, L. C. Jarrott, O. L. Landen, P. K. Patel, M. J. Rosenberg, and B. K. Spears, Phys. Plasmas **24** (2017).
[17] D. B. Thorn, A. MacPhee, J. J. Ayers, J. D. Galbraith, M. C. Hardy, N. Izumi, D. K. Bradley, L. A. Pickworth, B. Bachmann, O. L. Landon, M. B. Schneider, P. M. Bell, H. Y. Khater, J. D. Kilkenny, K. Hill, B. Kozioziemski, S. Person, C. A. Smith, S. Nagel, M. Bitter, and D. Clark, Proc. SPIE , 8 (2017).
[18] M. J. MacDonald, B. Kozioziemski, A. G. MacPhee, M. B. Schneider, J. Ayers, and D. B. Thorn, JINST **14**, P12009–P12009 (2019).
[19] L. Gao, B. F. Kraus, K. W. Hill, M. Bitter, P. Efthimion, M. B. Schneider, A. G. MacPhee, D. B. Thorn, J. Kilkenny, J. Ayers, R. Kauffman, H. Chen, and D. Nelson, Rev. Sci. Instrum. **89**, 10F125 (2018).
[20] R. Betti, M. Umansky, V. Lobatchev, V. N. Goncharov, and R. L. McCrory, Phys. Plasmas **8**, 5257–5267 (2001).
[21] H. A. Scott, JQSRT **71**, 689–701 (2001).
[22] M. J. MacDonald, D. A. Liedahl, G. V. Brown, D. Åberg, D. T. Cliche, M. E. Foord, P. E. Grabowski, R. F. Heeter, D. J. Hoarty, R. A. London, M. E. Martin, J. Nilsen, M. V. Patel, H. A. Scott, R. Shepherd, H. D. Whitley, and K. Widmann, Rev. Sci. Instrum. **93**, 093517 (2022).
[23] M. F. Gu, Can. J. Phys. **86**, 675–689 (2008).
[24] H. A. Scott and S. B. Hansen, HEDP **6**, 39–47 (2010).
[25] D. A. Mariscal, C. M. Krauland, B. Z. Djordjević, G. G. Scott, R. A. Simpson, E. S. Grace, K. Swanson, and T. Ma, Physics of Plasmas **29**, 093901 (2022).
[26] J. Svensson, M. von Hellermann, and R. W. T. König, Plasma Physics and Controlled Fusion **41**, 315 (1999).
[27] A. Pavone, J. Svensson, A. Langenberg, N. Pablant, U. Hoefel, S. Kwak, R. C. Wolf, and W. .-X. Team, Review of Scientific Instruments **89**, 10K102 (2018).
[28] A. Pavone, J. Svensson, S. Kwak, M. Brix, R. C. Wolf, and J. Contributors, Plasma Physics and Controlled Fusion **62**, 045019 (2020).
[29] L. L. Lao, S. Kruger, C. Akcay, P. Balaprakash, T. A. Bechtel, E. Howell, J. Koo, J. Leddy, M. Leinhauser, Y. Q. Liu, S. Madireddy, J. McClenaghan, D. Orozco, A. Pankin, D. Schissel, S. Smith, X. Sun, and S. Williams, Plasma Physics and Controlled Fusion **64**, 074001 (2022).
[30] A. Paszke, S. Gross, F. Massa, A. Lerer, J. Bradbury, G. Chanan, T. Killeen, Z. Lin, N. Gimelshein, L. Antiga, A. Desmaison, A. Köpf, E. Yang, Z. DeVito, M. Raison, A. Tejani, S. Chilamkurthy, B. Steiner, L. Fang, J. Bai, and S. Chintala, (2019), arXiv:1912.01703 [cs.LG].
[31] D. P. Kingma and J. Ba, (2017), arXiv:1412.6980 [cs.LG].
[32] D. Foreman-Mackey, D. W. Hogg, D. Lang, and J. Goodman, PASP **125**, 306–312 (2013).